
















Sulfur Implantation into Water Ice with Propane: Implications for Organic Chemistry on the Surface of Europa

Alexis Bouquet^{1,2} , Cíntia Aparecida Pires da Costa³ , Philippe Boduch³, Hermann Rothard³, Alicja Domaracka³ , Grégoire Danger¹, Isabelle Schmitz^{4,5}, Carlos Afonso^{4,5} , Philippe Schmitt-Kopplin^{6,7} , Vincent Hue² , Tom A. Nordheim⁸ , Alexander Ruf^{9,10} , Fabrice Duvernay¹ , Maryse Napoleoni¹¹ , Nozair Khawaja^{11,12} , Frank Postberg¹¹ , Thomas Javelle¹ , Olivier Mouis², and Laura Isabel Tenelanda Osorio¹³

¹ Aix Marseille Univ, CNRS, Institut Origines, PIIM, Marseille, France

² Aix Marseille Univ, CNRS, CNES, Institut Origines, LAM, Marseille, France

³ Centre de Recherche sur les Ions, les Matériaux et la Photonique CIMAP-CIRIL-Ganil, Normandie Univ, ENSICAEN, UNICAEN, CEA, CNRS, 14000 Caen, France

⁴ International Joint Laboratory—iC2MC: Complex Matrices Molecular Characterization, Total Research and Technology Gonfreville (TRTG), 76700 Harfleur, France

⁵ Normandie Université, COBRA, UMR 6014 et FR 3038, Université de Rouen-Normandie, INSA de Rouen, CNRS, IRCOF, 76130 Mont Saint Aignan, France

⁶ Helmholtz Zentrum München, Analytical BioGeoChemistry, Neuherberg, Germany

⁷ Technische Universität München, Chair of Analytical Food Chemistry, Freising-Weihenstephan, Germany

⁸ Johns Hopkins University Applied Physics Laboratory, Laurel, MD, USA

⁹ LMU Munich, Faculty of Physics, Schellingstraße 4, 80799 Munich, Germany

¹⁰ Excellence Cluster ORIGINS, Boltzmannstraße 2, 85748 Garching, Germany

¹¹ Freie Universität Berlin, Institute of Geological Sciences, Berlin, Germany

¹² Institute of Space Systems, University of Stuttgart, Germany

¹³ Geomicrobiology, Department of Geosciences, Eberhard-Karls-University Tuebingen, Schnarrenbergstrasse 94-96, 72076 Tuebingen, Germany; alexis.bouquet@univ-amu.fr

Received 2023 November 13; revised 2024 February 16; accepted 2024 February 28; published 2024 April 24

Abstract

We performed experiments of implantation of energetic sulfur ions (105 keV) into 2:1 water:propane ices at 80 K and analyzed the resulting refractory organic matter with ultrahigh-resolution mass spectrometry. Our goal was to characterize the organic matter processed in the surface conditions of Europa, where it would receive a heavy flux of energetic particles, including sulfur ions, and determine whether organosulfurs could be formed in these conditions, using the simplest alkane that can exist in solid form on Europa's surface. We find that the produced organic matter contains a large variety of both aliphatic and aromatic compounds (several thousand unique formulae), including polycyclic aromatic hydrocarbons (PAHs), with masses up to 900 amu. A large number of aromatic hydrocarbons is found along with oxygenated, mostly aliphatic, compounds. Organosulfurs are found in both CHS and CHOS form, demonstrating they can be formed from any organic compound through sulfur implantation. These organosulfurs' properties (aromaticity, mass) appear similar to the rest of the organic matter, albeit their low quantity does not allow for a thorough comparison. Our results have implications for the type of refractory organic matter that could be observed by the JUICE and Europa Clipper space missions and how the surface of Europa could generate complex organics, including PAHs and organosulfurs, that could then enrich the subsurface ocean. In particular, they indicate that a large diversity of organic matter, including organosulfurs, can be formed from simple precursors in a geologically short time frame under the ion flux that reaches Europa.

Unified Astronomy Thesaurus concepts: [Astrochemistry \(75\)](#); [Radiation interactions \(Ice\) \(2277\)](#); [Europa \(2189\)](#); [Galilean satellites \(627\)](#)

1. Introduction

Europa, the smallest of Jupiter's Galilean moons, likely hosts a salty liquid water ocean under its icy crust (Khurana et al. 1998; Kivelson et al. 2000). This ocean is likely in contact with the silicate interior, which could allow potential chemical disequilibria (powered by hydrothermal activity) favorable to life without need for sunlight (Chyba 2000; Chyba & Phillips 2001; Zolotov & Shock 2004), as has been observed on Saturn's moon Enceladus already (Postberg et al. 2009, 2011b; Hsu et al. 2015; Waite et al. 2017). The young surface (Bierhaus et al. 2009) and the presence of salts (Dalton et al. 2005; Ligier et al. 2016; Filacchione et al. 2019; Trumbo

et al. 2019; King et al. 2022) and sporadic geysers (Roth et al. 2014; Sparks et al. 2016; Jia et al. 2018) on this surface indicate that exchanges likely occur between the ocean and the surface, putting ocean material within reach of space instrumentation. These characteristics make Europa an especially attractive target for studies related to the developing field of astrobiology; as such, it will be the target of two ambitious space missions in the coming decade, ESA's JUICE (Grasset et al. 2013) and NASA's Europa Clipper (Howell & Pappalardo 2020). Both will carry high-resolution mass spectrometers to analyze volatile compounds of the exosphere (NIM, as part of the PEP instrument, and MASPEX, respectively), including those sublimating from surface features of special interest; Europa Clipper will also carry the Surface Dust Analyzer (SUDA) to investigate the grains ejected from the surface (Postberg et al. 2011a; Goode et al. 2023), which can give us insights on the refractory matter present. Due to the potential habitability of



Original content from this work may be used under the terms of the [Creative Commons Attribution 4.0 licence](#). Any further distribution of this work must maintain attribution to the author(s) and the title of the work, journal citation and DOI.

Europa, determining the composition of any organic matter that could be detected is a key objective, which requires investigating the factors that could affect the evolution of this matter on Europa's surface.

Europa is located in the inner magnetosphere of Jupiter. The volcanic activity of the innermost Galilean moon Io is a significant source of plasma in the Jupiter system: SO₂ emitted by the moon is dissociated and ionized by the energetic trapped electrons. The sulfur and oxygen ions then get picked up by the rotating magnetic field, accelerated close to the corotation velocity of the ambient plasma, and are radially transported outward, forming the Jovian plasma sheet (Thomas et al. 2004). Europa acts as an obstacle to the corotating flow of plasma and undergoes intense bombardment by energetic protons, electrons, and oxygen and sulfur ions (Cooper et al. 2001; Paranicas et al. 2002; Bagenal & Dols 2020). Because Europa is tidally locked and because its Keplerian velocity is slower than the corotating Jovian plasma, its trailing hemisphere is facing the incoming flow of Jovian plasma. To the first order, one would expect this hemisphere to experience stronger radiation weathering (Cassidy et al. 2013). However, predicting the exact magnitude and morphology of the precipitating charged particle flux reaching Europa is not trivial. It depends not only on the orientation of the background Jovian magnetic field, which varies with Europa's centrifugal latitude, but also on Europa's induced response to the interaction and the local electromagnetic perturbation around Europa. The flux is therefore highly spatially and temporally variable (Rubin et al. 2015; Addison et al. 2021; Harris et al. 2021; Nordheim et al. 2022).

The consequence is that any organic matter reaching Europa's surface from the interior would be processed by these radiations, which could induce extensive transformations, especially with other species (the ubiquitous water ice on the surface but also other compounds from ocean material) present to open new reaction pathways. The abundance of products would make it harder to draw conclusions on the ocean's composition based on observation of the organic matter present on the surface; investigations on the composition of organic matter processed under irradiation are therefore a prerequisite to interpret future measurements.

Another consequence of the surface radiation processing is the chemical enrichment of Europa with inorganic reactants. This includes the production of oxidants (Carlson et al. 1999a; Li et al. 2022), which, if returned to the ocean, could enhance its habitability by fostering redox disequilibria (Hand et al. 2007), and the "sulfur cycle," which results in the presence of large amounts of hydrated sulfuric acid on the trailing hemisphere (Carlson et al. 1999b, 2002; Strazzulla et al. 2007, 2009, 2023; Loeffler et al. 2011; Dalton et al. 2013; Ding et al. 2013; Li & Li 2023) and over sulfur-bearing species such as SO₂ (Becker et al. 2022). The diversification of organic matter is also an expected consequence of surface radiation chemistry. The presence of CO₂ on the surface of Europa, in temperature conditions where it should be quickly lost to sublimation, suggests that organic matter is being processed by surface radiations (Carlson et al. 2009).

Experimental work on the evolution of organic compounds under irradiation is abundant but tends to focus on conditions relevant to the interstellar medium (Oberg 2016) or comets (Moore & Hudson 1998) and therefore on temperatures lower than relevant for the Jovian moons' surfaces. Our group has

recently demonstrated that the same irradiation experiment performed at a higher temperature may yield different results (Tenelanda-Osorio et al. 2022), in this case with the higher temperature reducing the diversity of the volatile organic compounds formed. Experiments directly relevant to the surface conditions on Jovian moons have mostly focused on inorganic products (Moore & Hudson 2000; Carlson et al. 2002; Loeffler et al. 2006, 2011; Hand & Carlson 2015; Poston et al. 2017; Thomas et al. 2017; Davis et al. 2021; Li et al. 2022; Mifsud et al. 2022) or the destruction rate of possible biomarkers (Nordheim et al. 2018; Freissinet et al. 2019). One study investigated the formation of organic matter based on simple organic compounds in a water-ice matrix in conditions relevant to Europa (Hand & Carlson 2012). However, the refractory organic residues that were produced in these experiments could only be characterized through Fourier transform infrared (FT-IR) spectroscopy, which can only give an incomplete and coarse description of the content. Similarly, experiments involving sulfur tend to be rarer due to the practical difficulties involved with apparatus contamination (see Mifsud et al. 2021 for a review regarding experimental astrochemistry of sulfur); the ones that have been performed focus on the most abundant (and detectable, including in the Galileo spectral data) inorganic products rather than on sulfur's impact on organic chemistry (e.g., Strazzulla et al. 2007; Loeffler et al. 2011; Ding et al. 2013; Mifsud et al. 2022). Our group has previously investigated the effect of sulfur implantation in astrophysical ices (Ruf et al. 2019, 2021), i.e., in conditions relevant to colder, more remote objects such as comets or Kuiper Belt objects, than Europa's surface. Other work has shown the formation of sulfur-bearing organics in solution by photolysis of solutions containing S or S₂ and C₁₀H₂ (Heymann 2007).

In this work, we have investigated the result of irradiation with heavy ions (sulfur and argon) of water + propane ices. We chose propane because it is the simplest alkane that can be kept in solid form at a temperature relevant to Europa's surface; an alkane offers a good basis of comparison for future experiments involving organics bearing different functional groups (amines, carboxylic acids). We note that no carbon-bearing species other than CO₂ (Trumbo & Brown 2023; Villanueva et al. 2023) has been firmly detected on Europa's surface so far, but other organics are still likely to be present in surface material coming from the ocean, as suggested by Cassini observations at Enceladus (Postberg et al. 2018). Infrared features typical of organics are not as strong and discriminating as the CO₂ features around 2340 cm⁻¹, which, along with destruction under irradiation, would explain why their detection is more elusive than CO₂. Our goal was twofold: (1) characterize the organic residue left by the irradiation and sublimation of the H₂O:C₃H₈ ice to assess the possible complexity of organic matter formed on Europa's surface under the irradiation process and (2) determine if sulfur implantation can lead to organosulfur formation in conditions relevant to Europa's surface, and if so, whether these organosulfurs have any distinctive features that would separate them from potential sulfur-bearing organics coming from Europa's interior. In this study, we have performed ultrahigh-resolution mass spectrometry (UHRMS) on the organic residue, allowing a level of detail inaccessible through usual means like FT-IR.

In Section 2, we present the experimental methods for residue formation and the analytical pipeline used to determine

the composition of the residue. In Section 3, we describe the result of both the FT-IR and the UHRMS analysis. Section 4 discusses the interpretation of the results and their application to the context of Europa.

2. Methodology

2.1. Experimental: Production of Residues

The 2:1 water:propane samples were prepared in the IGLIAS device, which is described elsewhere (Augé et al. 2018). Briefly, IGLIAS is a ultrahigh vacuum chamber (down to 1×10^{-10} mbar) in which up to three windows can be cooled to temperatures as low as 9 K. To form a sample on a window, the desired mixture is introduced into the chamber in gas form through a needle that is translated near the targeted window. The mixture condenses onto the window, forming an icy layer. The deposited quantity is controlled through the loss of pressure in the ramp in which the mixture was prepared and then confirmed by the FT-IR spectrum of the newly formed sample. IGLIAS was connected to the ARIBE low-energy line of the Grand Accélérateur National d'Ions Lourds (National Large Heavy Ions Accelerator) facility in Caen, France. This line delivered the ion beam (Ar^{7+} or S^{7+} at a 105 keV energy) used to irradiate the samples. A diaphragm on the line and a mobile Faraday cup before the chamber were used to monitor the current; the diaphragm allows one to measure the current while the sample is being exposed to the beam, and the Faraday cup interrupts the beam. The ion flux varied slightly over the course of the experiment but stayed close to a value of $1 \times 10^{12} \text{ cm}^{-2} \text{ s}^{-1}$ (for both the Ar^{7+} and S^{7+} beams). The current measurement with the diaphragm was used to ensure that despite beam variation, each layer of the sample (see below) would be exposed to the same ion fluence as the first layer, which was 8.38×10^{14} ions. This fluence was obtained by subjecting the first layer to the beam for 30 mn. It was checked that this duration allowed the transition to a sputtering-dominated regime (see, e.g., Souza-Corrêa et al. 2019 for a breakdown of the terms describing the destruction of a sample under an ion beam). In this regime, the evolution of the chemical composition of the sample is limited, since the upper part of the layer is being eroded while deeper parts, previously untouched, start being affected.

The sample was monitored with a Bruker V70 FT-IR spectrometer. Reference backgrounds were acquired on each of the windows before deposition of the samples, both at room temperature and at 80 K. The IGLIAS device allows one to record FT-IR spectra (in transmission mode) of the sample while it is being exposed to the ion beam. During the irradiation, the destruction of propane was monitored through the evolution of the C–H stretching mode features between 2800 and 3000 cm^{-1} ; the ratio of propane to water was determined through the band strengths determined in Hudson et al. (2021). We note, however, that our spectra are influenced by the interaction of propane with water. This is noticeable, e.g., in the unique feature in the 1460–1480 cm^{-1} range, instead of the multiple peaks seen in Hudson et al. (2021) for pure crystalline propane. A similar change in this spectral region was observed by Ghosh et al. (2018) between pure crystalline propane and a 1:1 water:propane sample. However, since these authors did not determine band strengths for their mixture, we use the band strength given by Hudson et al. (2021) for the C–H stretch features in the 2800–3000 cm^{-1}

region. The water:propane ratio is equal to 2:1 in our deposits; i.e., it is comparable to the 3:1 ratio in the Hand & Carlson (2012) experiments. These experiments had shown that after irradiation at 80 K followed by heating to room temperature (causing sublimation of water, propane, and any volatile compound that had been produced), a refractory organic residue remains on the surface. To maximize the amount of residue for ulterior analysis, we performed multilayer irradiation: once the sample had been exposed to the desired fluence, a new layer of the mixture was deposited on top of it and then exposed to the ion beam until the same fluence was achieved. The process was repeated 15 times for each sample. The layer thickness, estimated through integration of the water 3200 cm^{-1} band to be more than 0.8 μm for each ice layer, ensures all ions are stopped in the newly deposited layer without reaching the previous one (maximum penetration depth estimated at 0.4 μm using the SRIM-TRIM software; Ziegler et al. 2010).

Two samples were prepared and irradiated: sample 1 was irradiated with the S^{7+} beam, and sample 2 was irradiated with the Ar^{7+} beam. They are hereafter referred to as W_S and W_{Ar} , respectively. These two samples underwent a very similar physical alteration (using SRIM-TRIM, Ziegler et al. 2010, we calculate argon's range and stopping power to be within 14% of sulfur's), but due to its reactivity, sulfur is susceptible to be included in the products formed after irradiation.

After irradiation of the 15 layers, the windows slowly heated up (0.5 K minute^{-1}) to 300 K, allowing for the volatile compounds to sublimate and leaving an organic residue on their surface. The windows were taken out of the chamber and kept under primary vacuum for later analysis of the residue (Sections 2.2.1 and 2.2.2).

2.2. Ultra-high-resolution Mass Spectrometry Analysis of the Organic Residues

2.2.1. Laser Desorption Ionization Fourier Transform Ion Cyclotron Resonance (LDI-FTICR)

Both the W_S and W_{Ar} residues were then analyzed through laser desorption ionization Fourier transform ion cyclotron resonance (LDI-FTICR) mass spectrometry at the COBRA laboratory in Rouen, France. The system is a hybrid quadrupole-FTICR Solarix XR from Bruker equipped with a 12 T superconducting magnet and a dynamically harmonized ICR cell. The mass spectrometer is also equipped with an electrospray ionization (ESI) source and a laser desorption ionization source (laser NdYAg $\times 3355$ nm). The FTICR-MS technique represents the highest mass resolving power ($R > 10^6$) and highest mass accuracy (< 200 ppb) among all mass spectrometric instruments (Ruf et al. 2017), allowing for determination of molecular formulae through combinatorial formula assignment. The samples, on their MgF_2 substrates, were introduced into the ionization source, ionized under LDI, and then transferred toward the paracell. MgF_2 substrates were preferred to the ZnSe substrates classically used in the IGLIAS setup, because previous attempts have shown that ZnSe substrates produce large ion clusters under LDI, thereby considerably degrading data quality. Multiple laser shots at different power settings were tried to determine the optimal laser power for ion production. The LDI parameters were as follows: laser shots, 600; and frequency, 2000 Hz with the laser power adapted to the sample. Indeed, the laser power is defined

by the minimum power to get signal to avoid the creation of artifacts (Maillard et al. 2018). It has been optimized for each sample.

The following ion transfer parameters were used for both ESI (see Section 2.2.2) in positive and negative ionization modes together with LDI analyses in positive ion mode: m/z 98–1200, capillary exit 150 V (–200 V in negative mode), deflector plate 200 V (–210 V in negative mode), funnell 150 V (–150 V in negative mode), skimmer1 25 V (–15 V in negative mode), funnel radio frequency (RF) amplitude 60 Vpp, octopole frequency 5 MHz, octopole RF amplitude 350 Vpp, lower cutoff of the quadrupole at m/z 120, time-of-flight (TOF) 1 ms, frequency TOF 6 MHz, TOF RF amplitude 200 Vpp, side kick offset –1 V (0 V in negative mode), and front and back trapping plate 1.75 V (–1.7 V in negative mode). In both LDI positive and ESI negative modes (the only ones for which data are presented in this paper), 200 scans were performed to acquire each spectrum.

The LDI ionization method has demonstrated its interest for untargeted analysis of organic samples that include an insoluble phase (Danger et al. 2020). As shown in anterior analysis, our residues all present an insoluble fraction (Section 2.2.2); therefore, LDI-FTICR gives the most complete overview of the sample. All LDI analyses were performed in the positive (hereafter LDI+) mode. Three replicate measurements were performed on each sample on a different part of the window. When time allowed, three replicates were run at two different laser power settings (16% and 18% of the maximum power). Blanks were performed on the “clean” part of the window (that was not exposed to deposition/irradiation). The data presented have been obtained with 18% of the laser maximum power, which was the lowest power that could reliably produce enough ions to gather spectra for both samples.

Calibration was performed in two steps. A first calibration list only including fullerene peaks (fullerenes being a usual by-product of LDI on organic samples) was used to do a first internal calibration. Then, other peaks were added to the list based on the annotations suggested by the Data Analysis (Bruker Daltonics Software) tool. Each of these new annotations were manually checked for the correct isotopic pattern. The updated list was used to perform a more precise internal calibration based on a linear model. The parameters of molecular formula attribution are described in Section 2.2.3.

2.2.2. Electrospray Ionization Fourier Transform Ion Cyclotron Resonance (ESI-FTICR)

The soluble phase of samples W_S and W_{Ar} were analyzed through ESI-FTICR at the COBRA laboratory. The soluble phase of the residues was extracted with methanol. A droplet of 50 μ l of methanol was deposited onto the window and then recovered; the operation was performed three times, to obtain 150 μ l of solution. This process left a refractory phase on the MgF_2 windows. Ulterior repetition of this procedure with toluene and dichloromethane showed that the remaining refractory phase could not be recovered with these solvents.

Extracted samples were then analyzed in both positive and negative modes. The ESI source parameters were as follows: capillary voltage 4200 V (4100 V in negative mode), nebulizer 2 bars (1 bar in negative mode), dry gas 4 L $minute^{-1}$, and dry temperature 180°C. We only present results obtained in the negative mode (hereafter ESI–) in this paper.

Calibration was performed in a similar way as with LDI-FTICR (see Section 2.2.1), with common fatty acids used in the

initial calibration list. Blanks were obtained by analyzing methanol that had been deposited on a MgF_2 window without residue. We note that when performing LDI-FTICR, the windows had to be held in the LDI cell with a piece of tape, whose glue could appear in the ESI analysis. To counteract this, our ESI blanks included analysis of methanol run on a clean MgF_2 window onto which a piece of the same tape had previously been applied and removed. These blanks featured a large number of peaks (see Appendix A, Figure 7); therefore, they were subtracted from the sample analysis spectra (after calibration of both) before any attempt to perform attributions was made.

2.2.3. Assignments of Molecular Formulae

Annotations were obtained with the following settings: the data analysis software was considering even and odd electron configuration ions (allowing for the assignment of radical species), the maximum error on the mass accuracy (see next paragraph) allowed was 0.4 ppm, and the “maximum formula” was $N_0 O_{10} S_1$ for LDI+ or $N_0 O_{20} S_1$ for ESI–, meaning that only annotations including no nitrogen, at most 10 (20) oxygen, and 1 sulfur were considered (carbon, nitrogen, and hydrogen are by default included in the search without any cap on their value).

After molecular formulae are obtained for every replicate measurement, only the annotations that were found in all three repetitions of the analysis on this sample are retained and presented in our results (Section 3.2) (in the case of an LDI+ analysis, the three repetitions at a given laser power are shown; for LDI+ analysis postextraction, only two repetitions were performed). For each formula, the error (the difference between observed m/z and calculated m/z , expressed in ppm) is calculated. Error versus m/z graphs are available in Appendix B, Figure 8, to show the quality of the calibration for each sample/ionization method type.

We also calculated the double-bond equivalent (DBE) of all annotations, with $DBE = \#C - \#H/2 + \#N + 1$. This quantity gives an indication of the number of double bonds and rings in the compound; the DBE versus $\#C$ graph allows comparison to values expected of polycyclic aromatic hydrocarbons (PAHs) and fullerenes.

3. Results

3.1. FT-IR

Due to the multilayer process we used, the interpretation of IR spectra is complicated by the presence of the anterior layers; moreover, once a few layers have been deposited, saturation becomes an issue. We therefore first focus here on the spectra taken after deposition and during irradiation of the first layer. Figure 1 (top) shows the spectrum acquired on a freshly deposited 2:1 water:propane layer, and a spectrum after this layer was submitted to 30 minutes of 105 keV S^{7+} irradiation, corresponding to a fluence of 8.38×10^{14} ions. This fluence was repeated for every layer. The reduction of the intensity of the features associated with propane (C–H bands at 1510–1356 and 3000–2830 cm^{-1}) is readily apparent. The notable new features appearing after irradiation indicate formation of CO_2 (2340 cm^{-1}), CH_4 (1302 cm^{-1}), and CO (2140 cm^{-1}) (Bouiloud et al. 2015); all three are common products of the irradiation of organic molecules in water ice.

For comparison with previous experiments on similar samples with electrons (Hand & Carlson 2012), we plot the evolution of the 2340 cm^{-1} feature linked to CO_2 , the

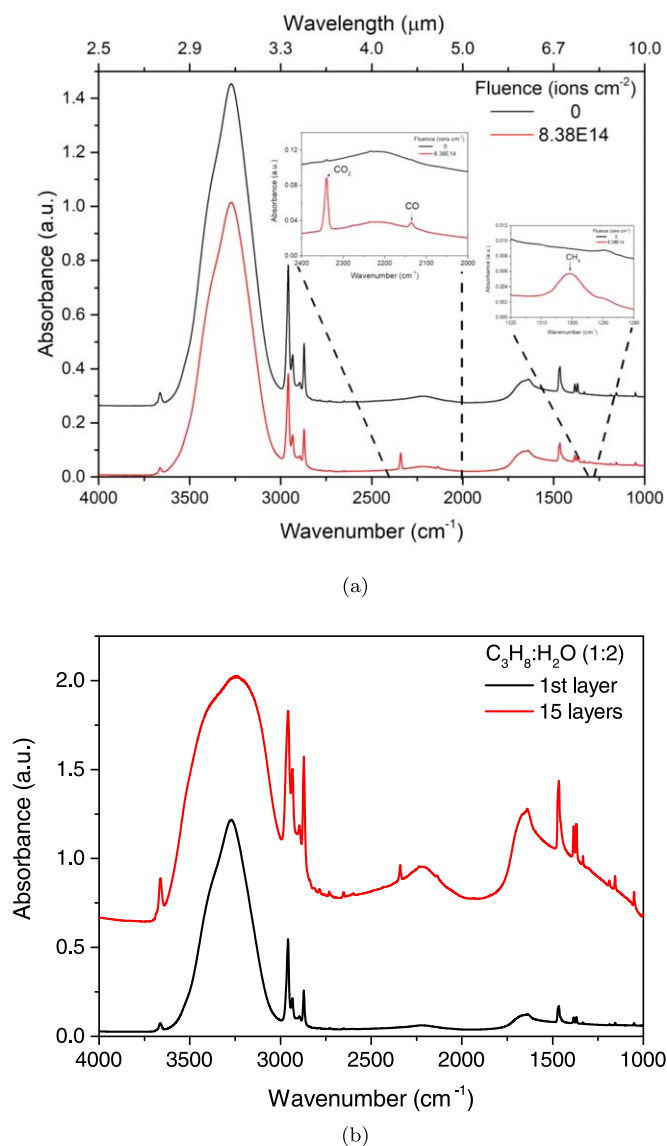


Figure 1. FT-IR spectra of a 2:1 water:propane mixture layer: Top: comparison between the sample after deposition (black) and after 30 min irradiation with S^{7+} ions (red). Bottom: comparison between the sample after deposition (black) and the spectrum of 15 similar layers, each individually irradiated with the 105 keV S^{7+} beam (red).

1302 cm^{-1} of CH_4 , and the $1510\text{--}1356$ and $3000\text{--}2830\text{ cm}^{-1}$ groups of bands due to C–H bonds (initially present because of propane). The evolution over the course of the irradiation is shown in Figure 2. Hand & Carlson (2012) report nearly simultaneous apparition of the CH_4 and CO_2 features, with CH_4 being the dominant feature until the higher doses; translated into abundances (using the band strengths provided in Gerakines et al. 1994 and Bouilloud et al. 2015), this indicates that CH_4 has been the most abundant of the two all along (by a factor of 5 at the highest dose). By contrast, in this work, CO_2 appears earlier, and the CH_4 integrated band absorption stays about 1 order of magnitude below the one of CO_2 . Quantification shows that once CH_4 is detectable, the CO_2/CH_4 ratio stays between 1.5 and 2. We also note that while Hand & Carlson (2012) did not see the 2140 cm^{-1} feature of CO in their irradiated spectra, it appears clearly in our experiments as shown in Figure 1; the CO_2/CO ratio tends toward 1.9 at the end of the experiment.

We now consider the spectra obtained after irradiation of the last (15th) layer (Figure 1, bottom). Due to the large total amount of material deposited on the window at this point, spectrum saturation becomes an issue for water- and propane-related features, as illustrated by the apparent deformation of the water OH stretching feature between 3000 and 3600 cm^{-1} ; however, the presence of multiple irradiated layers may allow for detection of the less abundant products.

A noticeable peak at 1643 cm^{-1} can be attributed to the C=C double bond stretching (Hudson et al. 2021). Similarly, the appearance of peaks at 999 and 1046 cm^{-1} is consistent with the formation of alkenes, with similar features in the spectrum of propene pure ice (Hudson et al. 2021) and water:propene ice (Hand & Carlson 2012). We note that in the experiments of Hand & Carlson (2012), these features were only visible when they directly formed these alkene-rich samples; their electron irradiation of alkanes did not yield such alkene features.

We also notice the appearance of two small features at 1929 and 1949 cm^{-1} , for which we did not find any possible assignment.

FT-IR spectra of Ar^{7+} irradiation experiments show no qualitative difference with S^{7+} irradiation and are not displayed, the latter showing no trace of features specific to sulfur-bearing products such as sulfuric acid (Strazzulla et al. 2007; Ding et al. 2013). This is expected, as the quantity of implanted S is small compared to the other elements in the sample; this was already observed in previous experiments by our group (Ruf et al. 2019).

3.2. UHRMS Analysis of the Residue

In this section, we describe the analysis of the refractory organic residue remaining on the sample holder using FTICR mass spectrometry. Section 3.2.1 covers the analysis of the whole residue using LDI, Section 3.2.2 covers the analysis of the soluble part of this residue using ESI, and Section 3.2.3 covers the LDI analysis of the insoluble part of the residue.

3.2.1. LDI+ Analysis

The LDI+ analysis of the W_S (sulfur-irradiated) sample yields 2076 unique annotations versus 2374 annotations for W_{Ar} (argon-irradiated). The overall intensity of peaks in the W_S acquisition is somewhat lower than for W_{Ar} (i.e., a peak for a given compound is smaller in W_S compared to its W_{Ar} counterpart), favoring the emergence of annotations for low-abundance compounds in W_{Ar} that would be lost in the noise in W_S .

During LDI+ acquisition, we noticed the samples were inhomogeneous, resulting in different intensities depending on the area at which the laser was aimed; while multiple replications mitigated the issue (with multiple acquisitions having to be interrupted for lack of sufficient signal to build up a spectrum over a given area), the intensity still differs between samples.

Figure 3 (top left and middle left panels) shows the DBE versus #C diagram of these annotations (see Section 2.2.3 for the definition of DBE). This figure only gives information related to the W_S sample; representation of data obtained on the W_{Ar} sample can be found in Appendix C, Figure 9.

Figure 3 shows that the refractory residue includes compounds with large numbers of carbon atoms, up to more

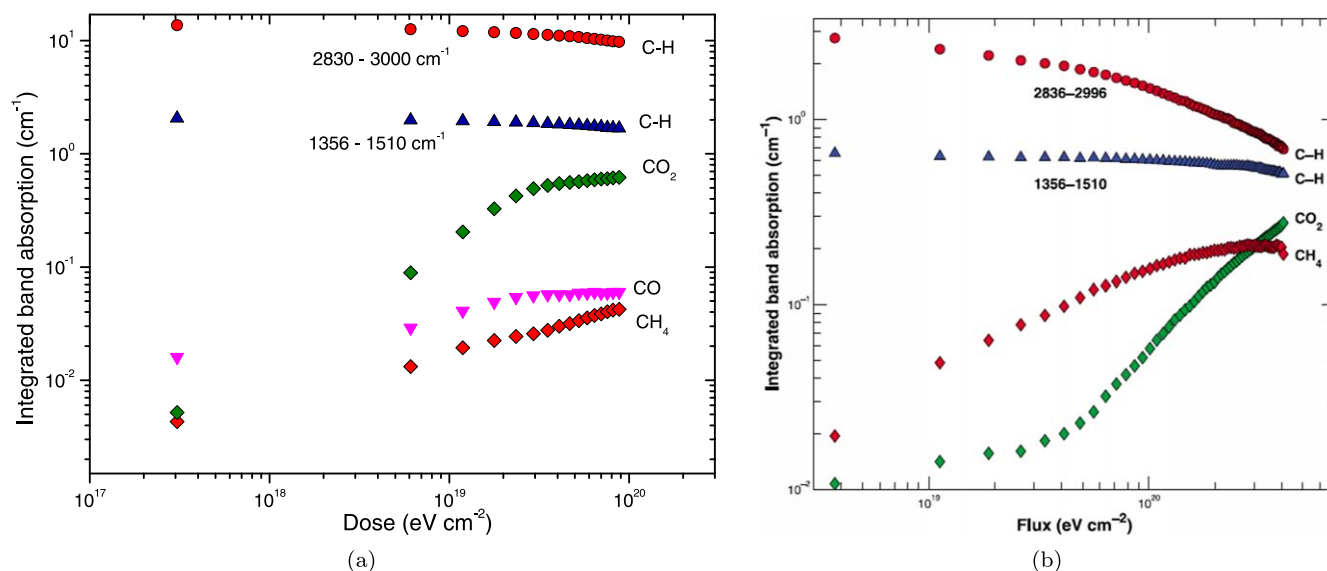


Figure 2. Evolution of the main features linked to CH_4 , CO_2 , and C–H bonds over the course of the irradiation of one layer of water:propane mixture with S^{7+} ions (left), compared to experiments with electrons (Hand & Carlson 2012; right, reproduced from the original paper).

than 70 (with m/z up to 900). The distribution is highly aromatic, with a significant number of annotations above the PAH limit. While this does establish the presence of numerous PAHs in our sample, one should also keep in mind that LDI ionization is favorable to the detection of aromatic compounds.

Oxygen-bearing products (CHO) are detected, following the same distribution as CH compounds, although they are more frequent at lower mass and DBE; this may be due to the overall lower intensity of all peaks at high mass/high DBE, which would make the O-bearing species (which are among the lowest intensity peaks) less detectable. Table 1 summarizes the relative weight (in intensity and number) of all five categories of annotations: C (fullerenes), CH, and CHO, as well as S-bearing CHS and CHOS. It shows that in both samples, CHO represents half of the annotations in number, but their intensity is lower (21.9% to 23.03%). We can also determine (Figure 3, bottom left panel) that the number of oxygen atoms $\#O$ in O-bearing compounds is at most two (the W_{Ar} sample shows 15 annotations at $\#O=3$, not displayed).

The number of S-bearing annotations in W_S is fairly modest in regard to the total number: only 35 out of 2076, with 34 being CHS compounds and only one being a CHOS. In comparison, W_{Ar} shows no S-bearing annotation at all despite the assignment method (Figure 9) being the same (individual measurements on this sample yield a few S-bearing annotations that do not overlap and are therefore eliminated in the final annotation list).

The identified CHS compounds appear to follow the overall distributions of other products in term of aromaticity (Figure 3, middle left panel), sitting for most of them on the PAH line. Their intensity is low, with all peak intensities being below 2×10^6 versus up to 10^8 for the whole distribution. This low intensity prevented confirmation of the assignment with isotopic patterns, as the additional peaks are drowned in the noise.

However, the difference between the number of S-bearing annotations in W_S and W_{Ar} , as well as the consistency between the CH/CHO distribution and the CHS one, indicates that organosulfur compounds are indeed present in the sample.

Table 1
Main Statistics on the Numbers and Types of Annotations

	LDI+		ESI−		LDI+ _{post}	
	W_S	W_{Ar}	W_S	W_{Ar}	W_S	W_{Ar}
N_{tot}	2076	2374	2686	3002	1840	2865
C	2.46/ 1.4	2.02/ 0.97	0	0	2.22/ 1.03	1.65/ 0.7
CH	75.35/ 47.64	74.95/ 47.01	0	0	73.82/ 48.48	62.27/ 40.31
CHO	21.88/ 49.28	23.03/ 52.02	98.18/ 94.30	99.75/ 99.83	23.77/ 49.57	31.03/ 58.74
CHS	0.3/ 1.64	0	0	0	0.15/ 0.82	0.02/ 0.1
CHOS	0.01/ 0.05	0	1.82/ 5.7	0.25/ 0.17	0.04/ 0.11	0.02/ 0.14

Note. N_{tot} is the total number of formulae obtained for the sample with this analysis method. For each type of compound, the percentage they represent in intensity (first number) and in number of annotations (second number) are given with regard to the total of all annotations. All these numbers are obtained with the “merged” measurements, i.e., by taking into account only formulae that appear in all three individual measurements for a sample/method (two measurements for LDI+_{post}).

3.2.2. ESI− Analysis

When proceeding to the extraction, a large part of the refractory residue did not dissolve and stayed on the MgF_2 window. This insoluble phase was then reanalyzed in LDI+ (see Section 3.2.3).

The ESI− analysis of the W_S sample resulted in 2686 unique annotations versus 3002 annotations for W_{Ar} . All annotations are oxygenated (see Table 1). This is consistent with the known behavior of ESI− analysis (favoring polar compounds) as well as the fact that methanol extraction would have recovered polar compounds preferentially.

The DBE versus $\#C$ graphs for W_S are given in Figure 3 (top right and middle right). The compounds detected with ESI

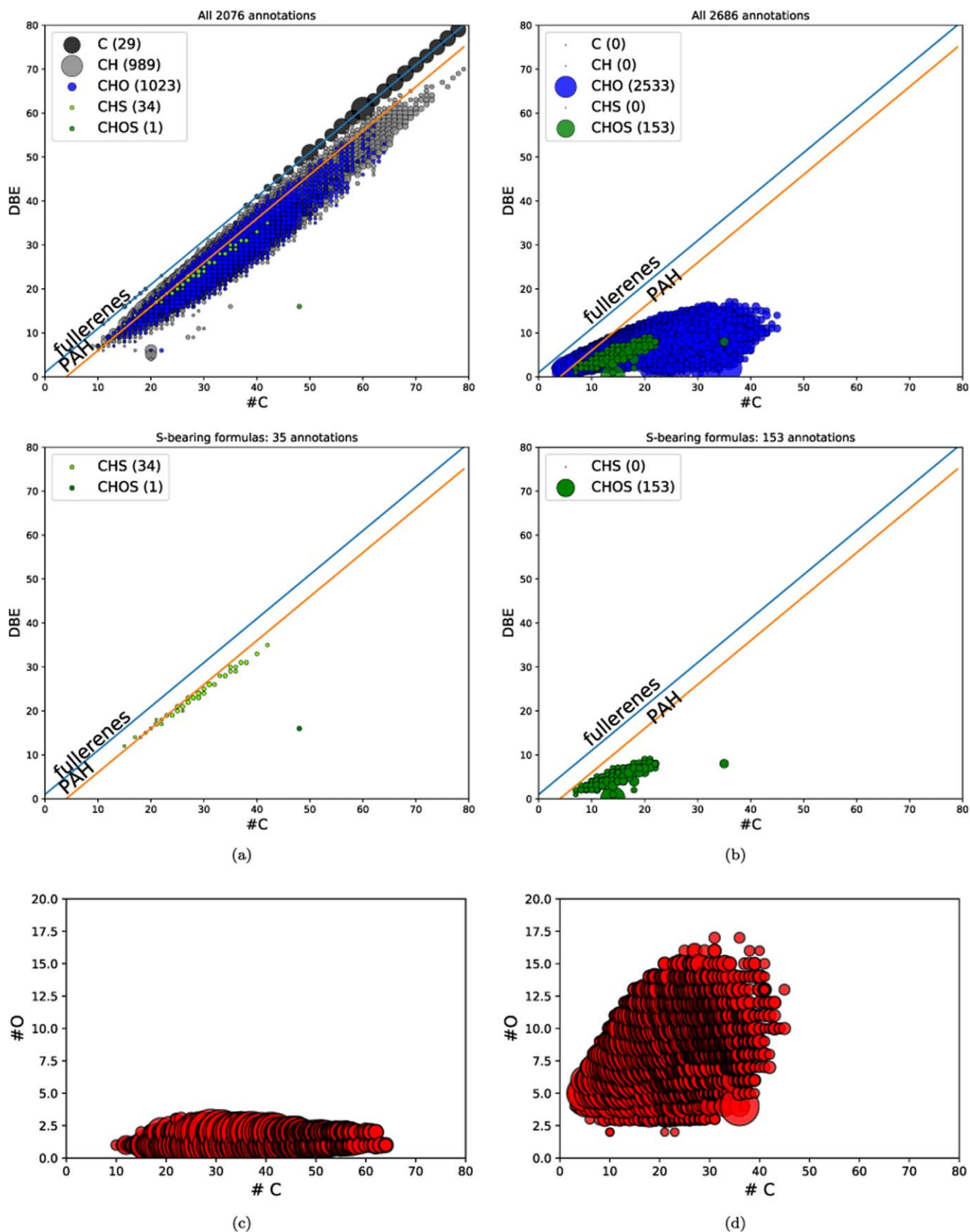


Figure 3. W_S sample, LDI+ analysis (left) and ESI- (right). The top and middle figures show the DBE vs. number of carbon atoms ($\#C$) in the formula for all annotations in a sample (top) and only S-bearing compounds (middle). The bottom figures show the number of oxygen atoms ($\#O$) vs. the number of carbon atoms ($\#C$). Note: dot size relates to the intensity of the formula in all graphs, but S-bearing compounds for the LDI+ analysis (middle left) have been enlarged for visibility.

– are much less aromatic, with a DBE versus $\#C$ distribution differing from the one seen in LDI+, overall well below the PAH line. The oxygen content is richer, with compounds showing up to 17 O atoms (Figure 3, bottom right).

ESI– analysis also indicates a relatively modest number of S-bearing annotations: 153 out of 2686 (5.7%), all CHOS (Table 1). The same analysis applied to the Ar-irradiated sample W_{Ar} yields five S-bearing annotations (0.17%). We checked these five annotations for their isotopic patterns and found that three of them are inconsistent and therefore are erroneous assignments. The two remaining annotations ($C_{10}H_{21}O_4S$ and $C_{11}H_{23}O_4S$) are consistent with alkyl sulfonic acids, common contaminants in ESI– analysis (Schmitt-Kopplin et al. 2010). The large difference in sulfur-bearing annotations between W_S and W_{Ar} leads us to infer that organosulfur compounds have been formed in W_S ; however, isotopic pattern verification was not possible due to low intensity. As with the LDI+ analysis, these organosulfurs are consistent in their DBE versus $\#C$ distribution with the rest of the annotations and are found among the lightest compounds ($C < 25$; Figure 3). The gap in total intensity between the S-bearing compounds and the complete population of annotations is less important than in LDI+, around 1 order of magnitude (versus 2 for LDI+), but S-bearing annotations nonetheless show a low intensity compared to other annotations (1.82% of the total). As a reminder, in previous experiments of sulfur implantation in water–methanol–ammonia ices at lower (20 K) temperatures, our group had found that 12% of the annotations bore sulfur (Ruf et al. 2019); we emphasize that in these experiments, the whole organic residue was soluble in methanol and could be analyzed in ESI–.

Again, the difference in S-bearing formulae between the W_S and W_{Ar} samples, as well as the distribution of these formulae, argues for the presence of organosulfur compounds resulting from the ion implantation into the W_S sample.

3.2.3. Postextraction LDI+ Analysis

Postextraction LDI+ analysis of the samples featured only two repeated measurements for each sample. The number of annotations obtained on the postextraction sample is not noticeably reduced, being even larger for W_{Ar} (Table 1). This observation should not be taken as evidence that W_{Ar} features more molecular diversity after extraction than before; one should keep in mind that we are discussing the “merged” measurements (see Section 2), which in the postextraction case include only two individual measurements instead of the three performed before extraction. This will lead to the elimination of fewer annotations in the postextraction case. Individual measurements for preextraction W_{Ar} produce 3063, 2812, and 3478 unique formulae versus 3112 and 3593 for postextraction W_{Ar} , supporting this interpretation.

The percentages of CH and CHO in the sample show very little evolution for W_S (2% less CH), but for W_{Ar} , CHO is more important postextraction (from 23.03% CHO before extraction to 31.03% after in intensity). This is counterintuitive, as extraction with methanol should have removed O-bearing compounds preferentially.

Figure 4 shows the DBE versus $\#C$ diagrams for W_S (left) obtained with LDI+ after extraction; it also shows the same diagram displaying only annotations that are common between the LDI+ pre- and postextraction analysis. The postextraction samples keep the same characteristics identified on the

preextraction samples in Section 3.2.1: high aromaticity, including a large number of compounds above the PAH line; relatively low intensity of the O-bearing annotations; and similar molecular weights. The right-hand side of Figure 4 emphasizes the similarity with the preextraction results by displaying the formulae that are common to pre- and postextraction analysis.

The number of CHS compounds in W_S is reduced in the postextraction analysis, with only 15 CHS annotations (versus 34 before extraction), all of them overlapping with at least one of the measurements of the preextraction analysis (11 overlap with the “merged” analysis; Figure 4, bottom diagrams). As with the preextraction LDI+ analysis, the CHS annotations are not intense enough to be verified through individual checks of isotopic patterns. On the other hand, two relatively intense CHOS annotations are present but can be dismissed as erroneous after an isotopic pattern check.

We note that postextraction, W_{Ar} also gives out three CHS annotations and four CHOS (see Appendix Figures 8 and 9); these formulae are all too weak in intensity to allow for isotopic pattern checking.

The difference between the number of S-bearing annotations in W_S and W_{Ar} (15 versus 7) is so small that no firm conclusion should be drawn as to the persistence of CHS compounds in the refractory phase of W_S after extraction of the soluble phase. The reduction in the number of CHS annotations with regard to the preextraction analysis may indicate that these CHS compounds could be removed by extraction; the remaining CHS in the postextraction data are among the heaviest compounds with the largest DBE (when compared to the CHS found in the preextraction analysis; Figure 4). On the other hand, we cannot be certain that all the methanol-soluble compounds have been extracted, as the insoluble phase may have retained some of them.

4. Discussion

4.1. Properties of the Organic Residue

First, it needs to be emphasized that the organic matter analyzed is the result of heating the irradiated samples. During heating, refractory precursors that do not sublime have opportunities to react at temperatures up to 300 K (final temperature of the sample holder). The timescales involved on the Jovian moons are much longer than that of our experiments, allowing for reactions normally inhibited by the low temperatures to occur; the heating of our samples may allow these reactions to occur in our experimental timescales. Also, the abundant presence of crystalline ice on Europa may be related to events heating the ice, such as melt-throughs (Greenberg et al. 1998; O’Brien et al. 2002; Ligier et al. 2016), indicating that compounds on the surface may have briefly experienced temperatures that could promote chemical reactions. However, the heating to 300 K may introduce biases by removing the volatile compounds, including the water-ice matrix, from the system and trigger reactions normally inhibited. Our results should therefore be understood as an indication of the organic precursors formed in the ice under ion implantation.

The results of our analysis show that in conditions relevant to Europa’s surface (80 K, abundant water ice), ion implantation can process even a light alkane compound into complex organic matter, with heteroatom transfer from the icy matrix leading to an important number of oxygenated compounds.

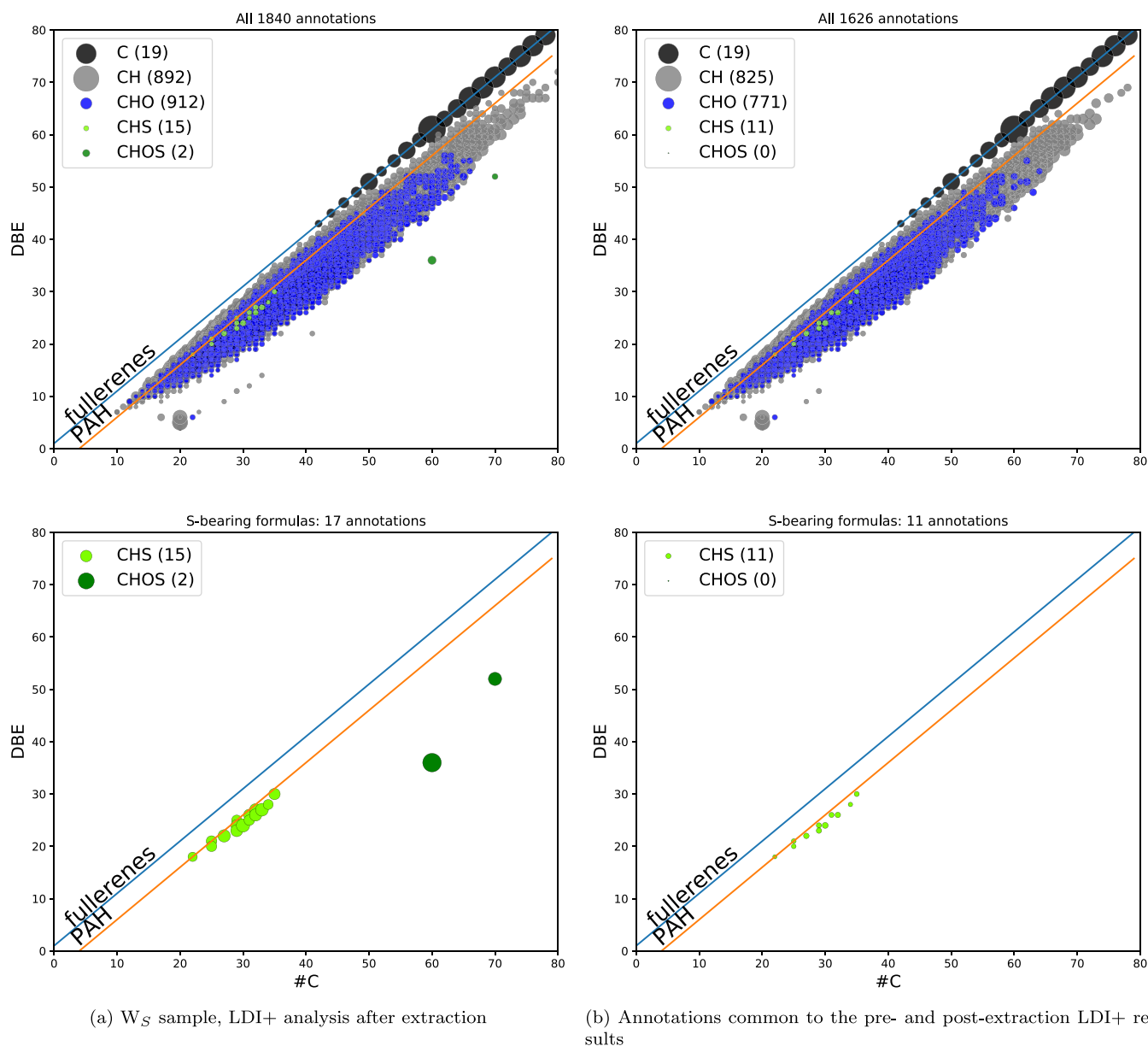


Figure 4. DBE vs. number of carbon atoms (#C) in the formula for all annotations (top) and only for S-bearing compounds (bottom). Note: while dot size relates to the intensity of the formula, S-bearing compounds have been enlarged for visibility.

LDI+ and ESI- ionization methods allowed us to find two different distributions of products, one aromatic (including PAHs) and oxygen-poor and the other more aliphatic and comparatively oxygen-rich. The large total number of annotations emphasizes the potential role of Europa's surface as a place of production of various organic products, including PAHs, and enrichment in heteroatoms (here, O coming from the water ice). Over time, this production may have played a role in the evolution of the organic content of the ocean. The products we detect span over a wide range of m/z values, from the practical limit of the FTICR at m/z 150 to more than 900. The formation of large organic compounds was likely favored by the relatively high abundance of propane compared to water in our irradiation targets. While the abundance of organics in Europa's ocean is expected to be orders of magnitude below water, we know of at least two mechanisms that would induce local concentration of organics. The first one is the formation of

an organic film at the top of the ocean, as has been inferred for Enceladus's own subsurface ocean (Postberg et al. 2018). The second one is slow freezing of brines on their way to the surface, which would segregate solutes and increase their concentration, as studied for salts (Naseem et al. 2023) and envisioned as an industrial process to concentrate organics, e.g., Baker (1967) and Kammerer & Lee (1969), who achieved it with considerably shorter freezing times than would occur on Europa. Therefore, ocean material reaching the surface could feature locally high concentrations of organics, for which the chemistry investigated in the present work is relevant.

Our main finding is the inclusion of sulfur in the products from ion implantation. The formation of organosulfurs by implantation has been demonstrated before (Ruf et al. 2019), however, at a lower temperature and in a mixture including an alcohol and ammonia. Here, the experiment is performed at a temperature relevant to Europa's surface; the only organic

involved is an alkane, and no ammonia is included. Our results therefore indicate it is likely that formation of organosulfurs through S implantation can occur from any organic on Europa's surface; no specific functional group in the precursor is required. Previous experiments have evidenced the formation of CHNOS compounds (Ruf et al. 2019); here, we show the formation of both CHOS and CHS compounds, indicating that organosulfur products can occur in multiple forms, which depend on the composition of the initial mixture. The higher number (and intensity) of CHOS annotations over CHS ones may, however, only reflect the relative ease of ionization with the selected ionization methods (LDI+ and ESI-) rather than a propensity to form CHOS more easily than CHS. The distribution of organosulfur compounds across all considered parameters (m/z , DBE) does not show a strong difference from the rest of the organic matter formed, but the number of detected S-bearing annotations is too small to draw firm conclusions in this regard. More experiments with larger amounts of sulfur are necessary to verify that organosulfurs formed by implantation on the surface of Europa would share the properties of the rest of the organic matter processed by radiation.

The similarity of the LDI+ postextraction results with the LDI+ preextraction indicates that the aliphatic, oxygenated, soluble phase is mostly inaccessible through ESI-, emphasizing the importance of complementary approaches in the analysis of such a complex organic matter.

We discuss the implications for detection and identification of similar matter on Europa's surface by future space missions in Section 4.3.

4.2. Applicability to Europa

Our experiments featured only one type of energetic projectile (S^{7+} or Ar^{7+} ions) and one projectile energy (105 keV). However, the complex and rich interaction between Europa, its tenuous atmosphere, and the magnetospheric plasmas results in an inhomogeneous incoming particle flux. At the highest energy (>1 MeV), the fluxes of precipitating magnetospheric ions are predicted to be rather uniform at the surface of Europa (Breer et al. 2019; Nordheim et al. 2022) and become increasingly asymmetric with decreasing energy.

Without accounting for the local electromagnetic field perturbation or for the ocean-induced field, the flux of magnetospheric plasma at the surface of Europa is expected to peak around the trailing hemisphere that faces the incoming flux of magnetospheric plasma. This creates a so-called bull's-eye pattern, with the highest fluxes on the trailing hemisphere (Cassidy et al. 2013).

The effect of the plasma interaction on the precipitating flux morphology was studied using an MHD simulation based on the BATS-R-US multifluid MHD code (Glocer et al. 2009). Rubin et al. (2015) solved the MHD equations in the case of three fluids (magnetospheric plasma, pickup ions from Europa, and electrons) and predicted an asymmetry in the plasma precipitating on Europa's surface between the sub- and anti-Jovian hemispheres.

Harris et al. (2021) went one step further and separated the ion fluids generated in Europa's atmosphere through the various physical processes into two fluids (O_2^+ and O^+), since they both have very different properties than the magnetospheric ion fluid. They also studied how the plasma interaction varied under different magnetospheric conditions as Europa

moves within the Jovian plasma sheet with Jupiter's rotation. Their predicted total precipitation rate for the thermal magnetospheric ions integrated over the entire Europa surface is in the range of $1.8\text{--}26 \times 10^{24} \text{ s}^{-1}$, corresponding to $5.9\text{--}84.7 \times 10^6 \text{ cm}^{-2} \text{ s}^{-1}$. This number was sensibly lower than those predicted by Cassidy et al. (2013), since Harris et al. (2021) accounted for the diversion of the upstream plasma flow around Europa. As Europa moves through the plasma sheet with Jupiter's rotation, the orientation of the background magnetic field vector also changes, which leads to shearing the bull's-eye pattern along the direction of the background magnetic field.

Accounting for the electromagnetic response of Europa to Jupiter's locally variable magnetic field modifies the predicted ion flux reaching the surface. Because of Jupiter's magnetic dipole tilt, Europa is immersed in a temporally variable background magnetic field, leading to a variation in its induced magnetic field from the conducting subsurface ocean over a Jovian rotation. Using particle tracing simulation combined with results from hybrid and multifluid MHD models, Addison et al. (2021) and Nordheim et al. (2022) found that the magnetic field line draping and pileup near Europa lead to significant changes in the morphology of the precipitating ion flux at the surface of Europa. Despite differences in the simulation input parameters (e.g., upstream plasma densities, atmospheric densities of Europa), these studies generally found a significant shielding around Europa's trailing hemisphere (facing the plasma flow) caused by the field line draping. This creates a significant redistribution of the precipitating particle flux at the leading hemisphere (downstream of the plasma flow) and an inverted bull's-eye pattern, i.e., an increased precipitating flux of the magnetospheric thermal ions at high latitude versus equatorial latitude. The extent of the exposed high-latitude region is more pronounced around the leading hemisphere (latitudes poleward of $\sim 45^\circ$) than around the trailing one (latitudes poleward of $\sim 25^\circ$).

The averaged flux of magnetospheric sulfur ions predicted at the high-latitude exposed regions from the combination of MHD models and particle tracing is given in Nordheim et al. (2022) as being in the $7.5 \times 10^9\text{--}1 \times 10^{10} \text{ cm}^{-2} \text{ s}^{-1}$ range for 1 keV sulfur ions and in the $6.7\text{--}9.0 \times 10^4 \text{ cm}^{-2} \text{ s}^{-1}$ range for 10 keV sulfur ions. For 100 keV sulfur, a region of high precipitating flux is also found near the equator around the anti-Jovian hemisphere, in addition to the high-latitude ones, with flux on the order of $2.0\text{--}3.0 \times 10^4 \text{ cm}^{-2} \text{ s}^{-1}$. At even higher energies, the flux of precipitating ions becomes slowly homogeneous across Europa's surface (see Figure 16 of Nordheim et al. 2022).

The fluence received by our samples is $8.38 \times 10^4 \text{ cm}^{-2}$ (as a consequence of our multilayer protocol, we obtained samples that are functionally equivalent to 15 cm^2 samples exposed to this fluence). This would be equivalent, considering the range of values expected at Europa for each representative energy (1, 10, and 100 keV), to 880–1330 yr for the 100 keV flux, 295–396 yr for the 10 keV flux, and 1–3 days for the 1 keV flux around the high-latitude region exposed to the precipitating ions, as well as the anti-Jovian hemisphere (at the very high energies). Note that the 1 keV flux would be implanted only in a much shallower layer of the surface; an SRIM (Ziegler et al. 2010) calculation gives an average range of 6.5 nm, with no projectile going beyond 15 nm. Inversely, deeper layers (below a few hundred nanometers) would be exposed to a steady

implantation of MeV sulfur ions, nearly independently of the location on the surface. The range of 1 MeV S ions in water ice is calculated with SRIM to be $2 \mu\text{m}$. The 1 MeV flux given in Nordheim et al. (2022), in the $1\text{--}1.3 \times 10^3 \text{ cm}^{-2} \text{ s}^{-1}$ range, would mean the fluence of our experiments is reached in around 10^5 yr, which is still a short time in geological terms.

These orders of magnitude show that our experiments are more applicable to “recently” deposited materials (e.g., from cryovolcanic activity) rather than the long-term evolution of the most heavily irradiated regions or deeper (but still accessible to remote observations) layers reached by the most energetic ions.

The 80 K temperature chosen in these experiments falls well within the possible range of temperatures at relatively high latitudes, where the relative importance of the ion flux compared to electrons is higher (Nordheim et al. 2022). Values as low as 46 K have been proposed for the annual average at the poles versus 86 K at the equator (Ashkenazy 2019). Observations encompassing only lower latitudes yielded a range of 86–132 K (Spencer et al. 1999). We note that while our experiments were conducted at temperatures too low to be relevant to Callisto (with surface temperatures of the order of 150 K; Carlson 1999), sulfur-bearing carbon compounds possibly resulting from sulfur implantation have been detected on its surface, with features that could be due to CS_2 and OCS (Cartwright et al. 2020). Organic chemistry induced by sulfur implantation is likely on the surface of the other Galilean moons.

4.3. Implications for Future Observations

Complex organic matter will be a target of interest of Europa Clipper’s instruments, especially SUDA (Kempf et al. 2023, under review), which can investigate refractory materials inside icy dust grains ejected from the surface by the ambient micrometeoroid bombardment (Miljković et al. 2012). The capability to characterize complex organic material has already been demonstrated with organic species in ice grains emerging from Enceladus’s ocean using SUDA’s predecessor instrument, the Cosmic Dust Analyser (CDA; Postberg et al. 2018; Khawaja et al. 2019). Compared to CDA, SUDA has a superior performance and can measure TOF mass spectra of both positive and negative ions after impact ionization of these dust grains, where the negative ion mode favors the detection of those compounds that can be easily deprotonated, e.g., carboxylic acids, organosulfates, and organonitrates. It has been demonstrated previously (Klenner et al. 2019) that impact ionization produces similar ions as ionization by laser desorption, and thus the LDI mass spectra of this work can be seen as good guidance for SUDA. Laboratory experiments with analog materials have shown that polar organic compounds, such as amino acids, appear with the highest sensitivity in cation mode, whereas large molecules with low polarity, like fatty acids, have a tendency to be better observed in anion mode (Klenner et al. 2020a, 2020b; Napoleoni et al. 2023a, 2023b; Dannenmann et al. 2023). Analog experiments performed with a range of organics in sulfate- and sulfuric-acid-rich matrices showed that organics are detectable by SUDA in the form of molecular ions and adducts, with higher sensitivity in either cation or anion mode depending on the functional groups and properties of the organics (Napoleoni et al. 2023a). The results of the present study indicate that positive ions alone already provide a huge variety of organic species, the complexity of which will be challenging to SUDA

with a mass resolution of about 200 (Kempf et al., under review). However, the repetitive patterns with high signal-to-noise apparent in our mass spectra (Figure 6) will be easily detectable with SUDA allowing for the identification of the dominating species. Moreover, recording both cation and anion spectra will help to resolve many remaining ambiguities. Since some species have a strong signal up to at least m/z 900 (Figure 6), it seems to be advisable to occasionally extend the default SUDA mass range (1–500 amu) to higher masses to assess the composition of the most massive organic species. Preliminary work indicates SUDA will likely be capable of distinguishing S-bearing organics. Analog mass spectra for the SUDA instrument were recorded for a S-bearing organic compound, p-toluene sulfonic acid ($\text{C}_7\text{H}_8\text{O}_3\text{S}$), with laser-induced liquid beam ion desorption (LILBID) coupled to TOF mass spectrometry (Figure 5). The LILBID technique allows an accurate simulation of the spectra of SUDA-type impact ionization mass spectrometers (Klenner et al. 2019). The cation mass spectra (Figure 5) show that p-toluene sulfonic acid is clearly identifiable thanks to a protonated molecular peak at m/z 173 and several characteristic fragments of the organic compound, e.g., $[\text{M-OH}]^+$ (m/z 155), $[\text{M-HSO}_3]^+$ (m/z 91), and protonated benzene (m/z 79).

5. Conclusion

We have performed 105 keV sulfur ion implantation into 2:1 water:propane ices at 80 K and have analyzed the resulting organic residue to characterize the organic content and determine whether sulfur-bearing organics were formed.

We found that the organic residue featured a large organic diversity, with compounds with m/z values up to 900, thousands of unique formulae for each ionization method used, and a large number of O-bearing annotations. The residue features both aliphatic and highly aromatic compounds. The organic residue includes an insoluble phase in which compounds with highest degree of aromaticity are found.

Sulfur-bearing organic compounds are detected in both the insoluble and soluble phases. While their small number makes a comparison challenging, they do not appear to depart from the distribution of other formulae. Both CHS and CHOS compounds are present; the latter are found in larger numbers, which could be due to biases introduced by the ionization methods.

Since the number of implanted elemental sulfur ions is modest compared to the total content of the sample (less than 1×10^{15} sulfur ions distributed over a thickness of about $0.3 \mu\text{m}$), the detection of these products indicates that S is relatively easily integrated into the organic chemistry triggered under irradiation, and that it can occur starting from any organic compound, without any need for a specific functional group. The small number of implanted elemental ions also meant it was not possible to evaluate whether inorganic sulfur-bearing species, such as sulfuric acid (Strazzulla et al. 2007; Ding et al. 2013), were formed.

Our experiments were performed at 80 K, a temperature relevant to the midlatitude regions of Europa. The dose deposited (and number of implanted ions) corresponds to a fairly short period on Europa’s surface (measured at most in thousands of years). The results indicate that formation of a large diversity of organic matter from simple precursors, and of sulfur-bearing organics, can occur in this relatively short time frame. This is especially relevant to measurements from future

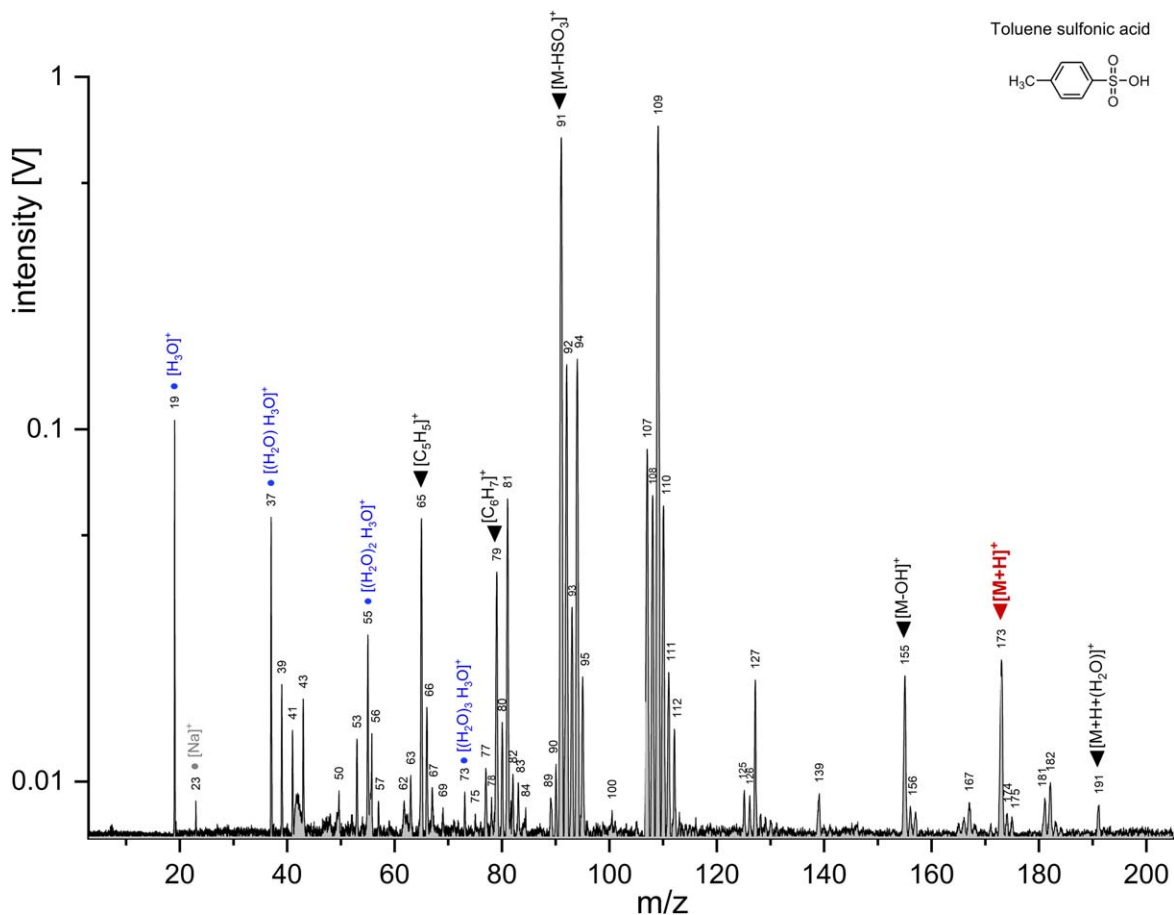


Figure 5. Cation LILBID mass spectra of p-toluene sulfonic acid, recorded at a concentration of 0.05 mol L^{-1} in a pure water matrix, simulating the mass spectra of SUDA on board the Europa Clipper.

space missions at Europa: recently deposited materials are our best window into the interior's composition, especially the ocean, and therefore would be priority targets of these investigations. Due to the apparent irregularity of Europa's activity (Roth et al. 2014; Sparks et al. 2016; Jia et al. 2018), there is no certainty that space missions will get a chance to examine material that has not been altered through radiation processing.

Complex organic matter will be a target of interest of Europa Clipper's instruments, especially SUDA, which can investigate refractory materials ejected from the surface. Our results show that precursors for complex organic matter, including high-mass compounds with PAHs, can be generated under a fairly modest dose, with inclusion of heteroatoms provided by the particle bombardment. The kind of matter formed in this study would generate challenging spectra in SUDA, possibly requiring adaptation of the instrument settings (e.g., punctual extension of the mass range) to better characterize it.

Future experiments should investigate the organic diversity that can emerge from precursors bearing various functional groups (alcohol, carboxylic acid, amine) in order to determine whether this leads to a marked difference in the resulting products. In the case of the Jovian moons, this would tell us how processed organic matter can reflect the precursors coming from the interior. Species that are deemed by geochemical models to be indicative of the ocean's state (pH, redox couples) should be prioritized. Since the only carbon-bearing species whose presence is established on Europa is CO_2 (Carlson et al.

2009; Trumbo & Brown 2023; Villanueva et al. 2023), the question naturally arises of what organic diversity could result from its radiation processing. Irradiation experiments of water + CO_2 samples have yielded a variety of products, overwhelmingly oxidized, including CO, formaldehyde, light alcohols, and carboxylic acids (Pirronello et al. 1982; Moore & Khanna 1991; Moore et al. 1991; Brucato et al. 1997; Bennett et al. 2010; Pilling et al. 2010; Jones et al. 2014; Petrik et al. 2014). However, it is important to note that these experiments have been performed at low temperatures (30 K or below); the higher temperatures of Europa's surface would promote escape of CO and H, thereby reducing the yields of CO_2 radiation chemistry and accentuating the oxidizing conditions in the irradiated water-ice matrix. The formation of complex organic matter including long aliphatic chains or multiple cycles seems unlikely in these conditions. Experiments of sulfur implantation into CO_2 ices (Lv et al. 2014; Mifsud et al. 2022, 2023) have yielded some of the usual oxidized products of CO_2 radiation processing, but the absence of hydrogen in these experiments meant that no hydrogenation of carbon could occur.

Experiments involving larger amounts of sulfur (whether as ions or as S-bearing species already present in the sample) should also be performed for a more thorough understanding of the characteristics of the produced organosulfur compounds. The behavior of other heteroatoms, such as N coming from hypothetical NH_3 or chlorine being implanted as energetic particles coming from Io (Küppers & Schneider 2000), should

also be investigated to determine the range of diverse organic matter that could be formed on the surface of Europa, Ganymede, and Callisto. Parameters such as dose and temperature also need to be explored for completing our understanding of these processes depending on surface location. Since electrons represent a large flux of energy onto Europa's surface (Addison et al. 2023), experiments also need to focus on them, although since energetic ions distribute a large amount of their energy through secondary electrons (Rothard et al. 2017), the resulting processes and products are expected to be similar, albeit individual yields would likely be different (e.g., Teolis et al. 2017).

Acknowledgments

Financial support from the IR INFRANALYTICS FR2054 for conducting the research is gratefully acknowledged. The experiments were performed at the Grand Accélérateur National d'Ions Lourds (GANIL) by means of the CIRIL Interdisciplinary Platform, part of CIMAP laboratory, Caen, France. We thank the staff of CIMAP-CIRIL and GANIL for their invaluable support. This work was supported by CNES, focused on the JUICE mission. This work was supported by the Programme National de Planétologie (PNP) of CNRS-INSU cofunded by CNES. We acknowledge support by the Region Normandie (RIN SCHINOBI) including a postdoc grant for CAFDC. A.B. and V.H. acknowledge support from the French government under the France 2030 investment plan, as part of the Initiative d'Excellence d'Aix-Marseille Université—A*MIDEX AMX-21-PEP-032 and A*MIDEX AMX-22-CPJ-

04, respectively. The project leading to this publication has received funding from the Excellence Initiative of Aix-Marseille Université—A*Midex, a French "Investissements d'Avenir program" AMX-21-IET-018. This project received support from the project FACOM (ANR-22-CE49-0005-01_ACT), funded by l'Agence Nationale de la Recherche (ANR) under the Generic Call for Proposals 2022. We acknowledge the funding from ANR IGLIAS grant ANR-13-BS05-0004 of the French Agence Nationale de la Recherche".

Appendix A Raw Spectra and Blanks

Figure 6 shows the FTICR spectra obtained for W_S for LDI+, ESI-, and LSI+ after extraction, as displayed by the Bruker Daltonics Data Analysis software used for the analysis.

Figure 7 shows the FTICR spectra of one of each blank (blanks were performed twice). The first one was performed for the LDI+ analysis (laser shots on a sample-free part of the MgF_2 window); it was not subtracted from the sample LDI+ spectra since its peaks are not numerous and have very low intensity (which would also preclude from calibrating it properly before subtraction).

The second blank was subtracted from ESI spectra before performing formula attributions. This blank includes the methanol that was used for the sample extraction and injection into the ESI, as well as the soluble (in methanol) part of the glue from the tape used on the windows during the LDI analysis.

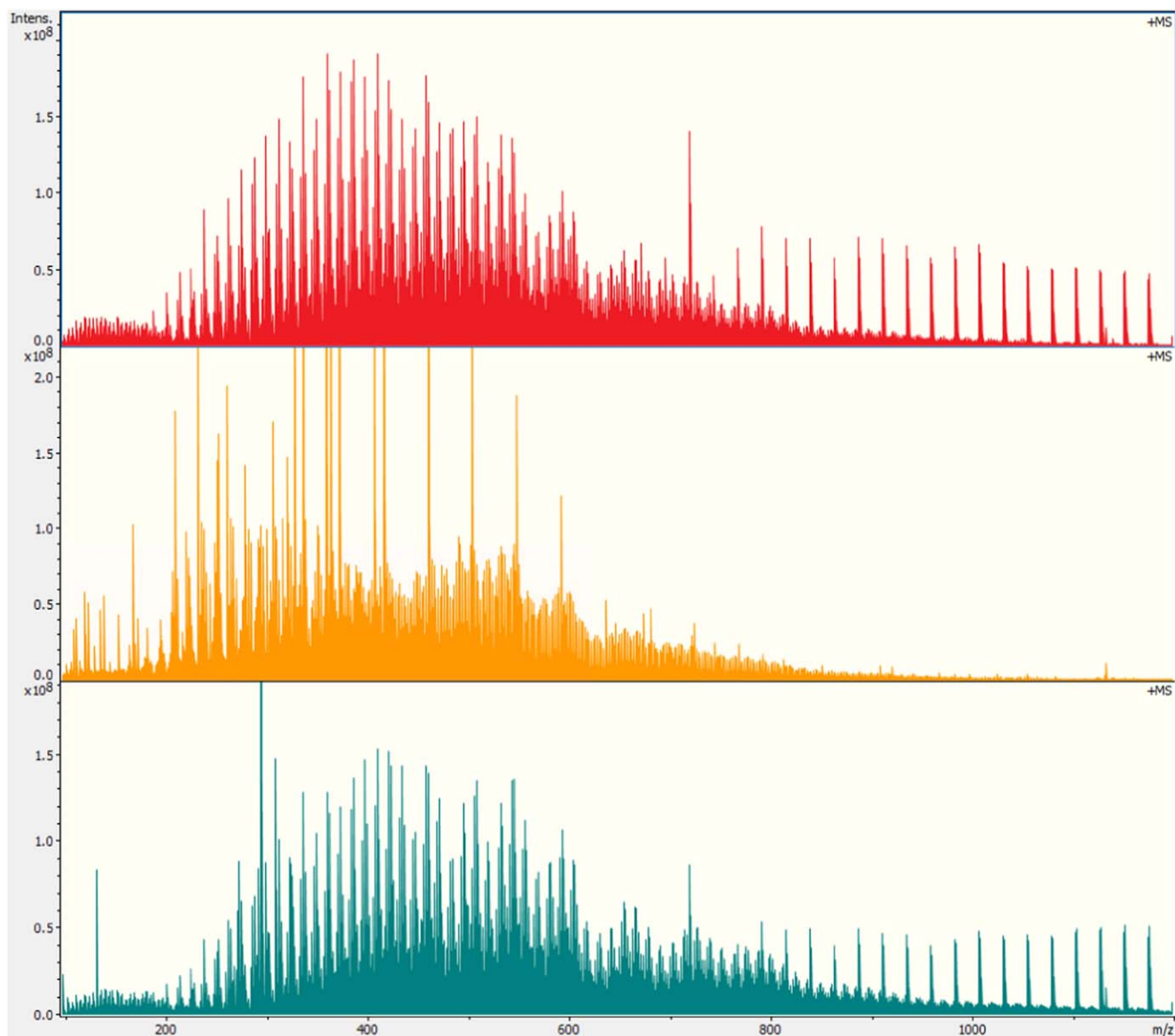


Figure 6. Raw FTICR spectra obtained for W_S with LDI+ (top), ESI- (middle), and LDI+ postextraction (bottom). The scale has been chosen to allow comparison of the main distributions but cuts off some large intensity peaks (mostly fatty acid contaminants in the ESI- spectrum). The repetitive peaks above m/z 800 in the LDI+ spectra are fullerenes, which are a by-product of the LDI process (this includes the large peak at 720, which is C60).

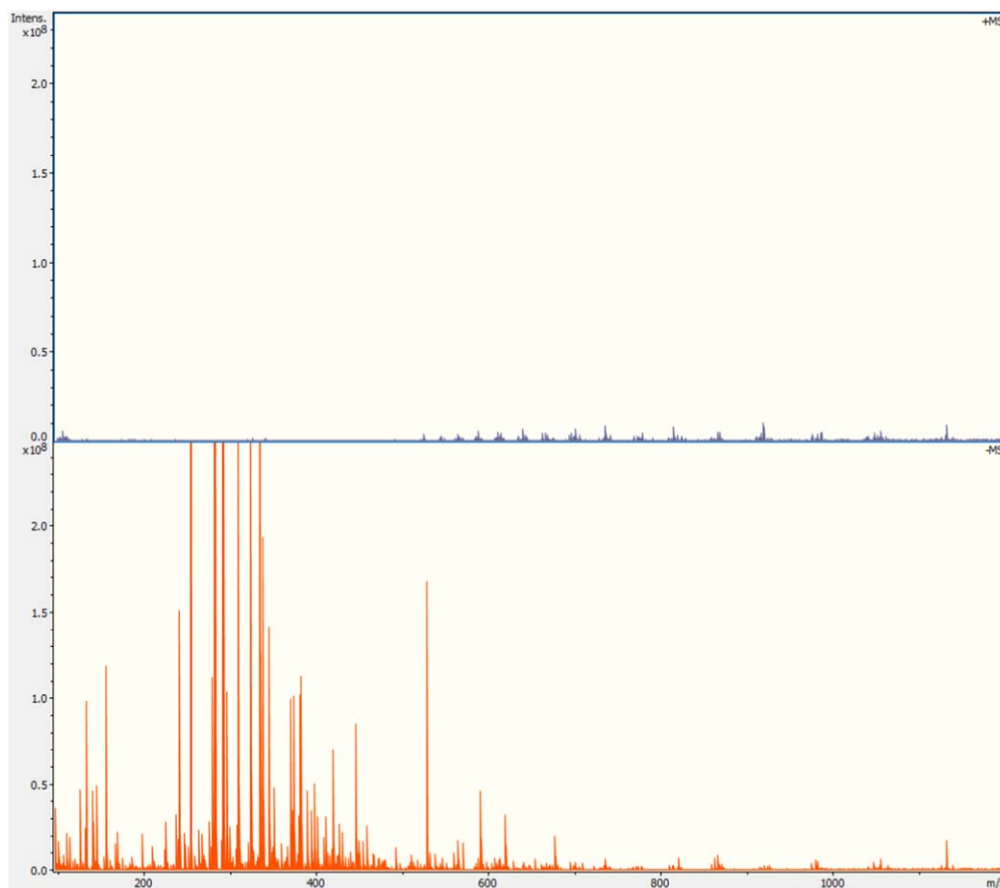


Figure 7. Example of blanks. Top: LDI+ blanks, obtained with laser shots aimed at the sample-free part of the window. Bottom: blank obtained with methanol that was deposited on a MgF_2 window on which tape (that was used to hold the sample windows in the LDI cell) was applied and removed.

Appendix B Error Plots

Figure 8 displays the error versus m/z plot for both samples W_S and W_{Ar} . Errors are displayed in ppm of the theoretical

formula. These plots show the quality of the calibration. With an error mostly contained within ± 0.2 , the calibration appears satisfactory.

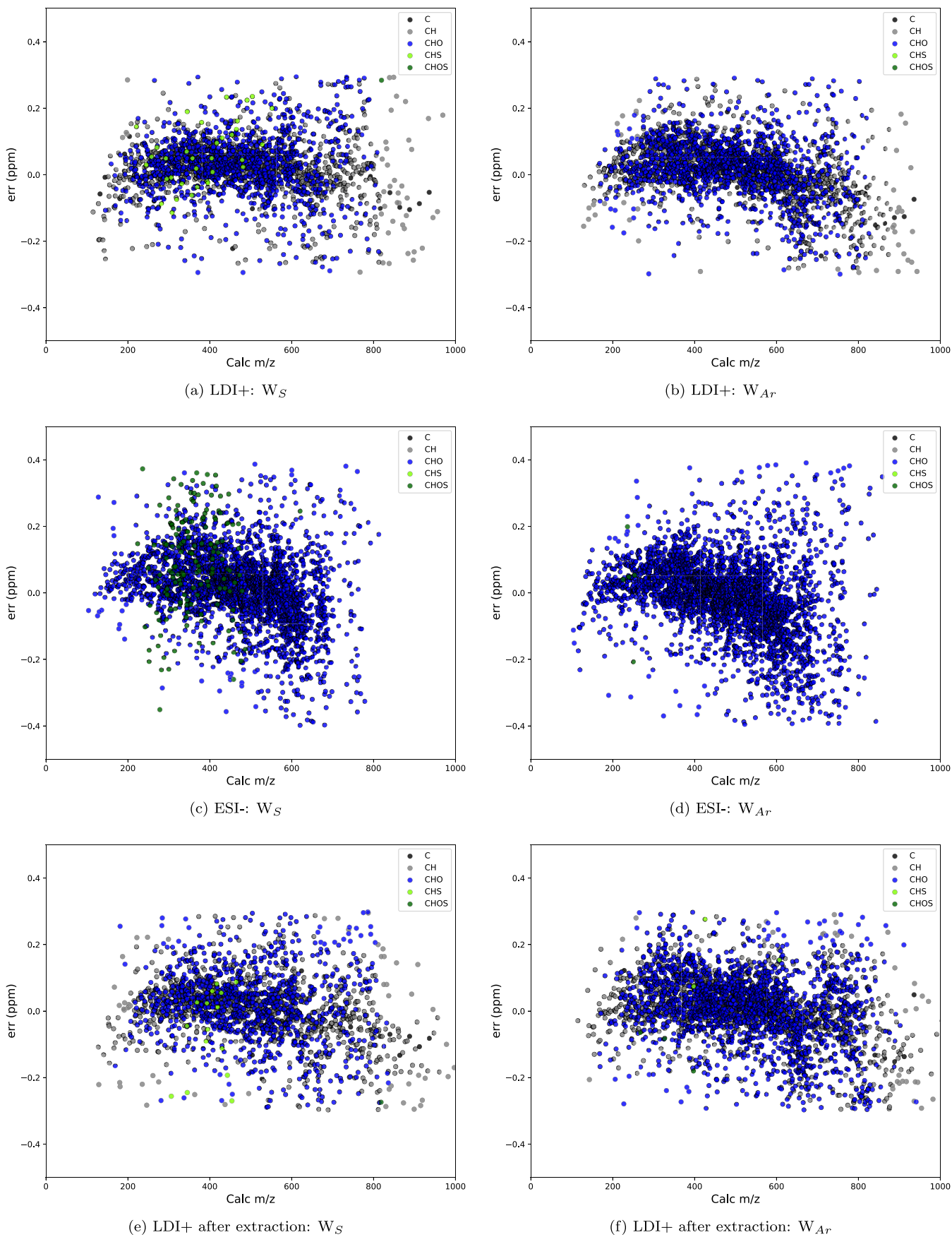


Figure 8. Error (in ppm) vs. m/z graph for W_S (left) and W_{Ar} (right), with LDI+ (top), ESI- (middle), and LDI+ after extraction (bottom).

Appendix C W_{Ar} Plots

Figure 9 shows DBE versus #C plots for the W_{Ar} sample to allow comparison with the plots displayed earlier for W_S. The

distribution are similar, but W_{Ar} appears to have more numerous formulae. The presence of S-bearing formulae is discussed in the main text.

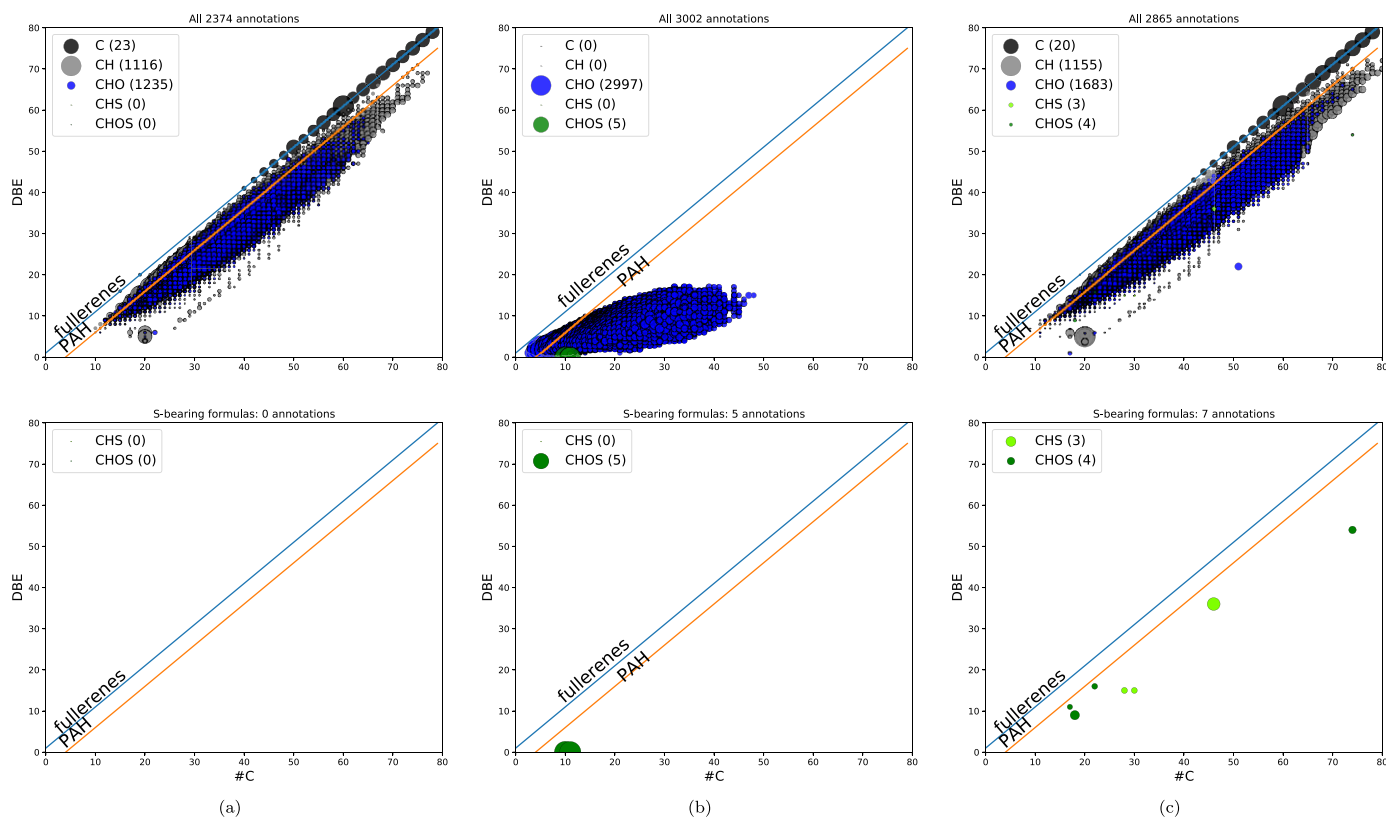








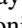






Figure 9. W_{Ar} sample: DBE vs. number of carbon atoms (#C) in the formula for all annotations in a sample (top) and only S-bearing compounds (bottom), LDI+ analysis (left), ESI- (middle), and LDI+ after extraction. Note: while dot size relates to the intensity of the formula, S-bearing compounds for the LDI+ analysis (bottom left, bottom right) have been enlarged for visibility.

ORCID iDs

Alexis Bouquet  <https://orcid.org/0000-0001-8262-9678>
 Cíntia Aparecida Pires da Costa  <https://orcid.org/0000-0001-7983-4590>
 Alicja Domaracka  <https://orcid.org/0000-0003-1585-2436>
 Carlos Afonso  <https://orcid.org/0000-0002-2406-5664>
 Philippe Schmitt-Kopplin  <https://orcid.org/0000-0003-0824-2664>
 Vincent Hue  <https://orcid.org/0000-0001-9275-0156>
 Tom A. Nordheim  <https://orcid.org/0000-0001-5888-4636>
 Alexander Ruf  <https://orcid.org/0000-0002-0383-4292>
 Fabrice Duvernay  <https://orcid.org/0000-0002-5056-3106>
 Maryse Napoleoni  <https://orcid.org/0000-0002-7988-6523>
 Nozair Khawaja  <https://orcid.org/0000-0001-8237-1523>
 Frank Postberg  <https://orcid.org/0000-0002-5862-4276>
 Thomas Javelle  <https://orcid.org/0009-0004-2471-7740>

References

- Addison, P., Liuzzo, L., Arnold, H., & Simon, S. 2021, *JGRA*, **126**, e29087
 Addison, P., Liuzzo, L., & Simon, S. 2023, *JGRA*, **128**, e2023JA031734
 Ashkenazy, Y. 2019, *Heliy*, **5**, e01908
 Augé, B., Been, T., Boduch, P., et al. 2018, *RSci*, **89**, 075105
 Bagenal, F., & Dols, V. 2020, *JGRA*, **125**, e27485
 Baker, R. A. 1967, *WatRe*, **1**, 61
 Becker, T. M., Trumbo, S. K., Molyneux, P. M., et al. 2022, *PSJ*, **3**, 129
 Bennett, C. J., Jamieson, C. S., & Kaiser, R. I. 2010, *PCCP*, **12**, 4032
 Bierhaus, E. B., Zahnle, K., Chapman, C. R., et al. 2009, in Europa, ed. R. T. Pappalardo, W. B. McKinnon, & K. K. Khurana, 161 (Tucson, AZ: Univ. Arizona Press)
 Bouilloud, M., Fray, N., Bénilan, Y., et al. 2015, *MNRAS*, **451**, 2145
 Breer, B. R., Liuzzo, L., Arnold, H., Andersson, P. N., & Simon, S. 2019, *JGRA*, **124**, 7592
 Brucato, J. R., Palumbo, M. E., & Strazzulla, G. 1997, *Icar*, **125**, 135
 Carlson, R., Anderson, M., Johnson, R., Schulman, M., & Yavrouian, A. 2002, *Icar*, **157**, 456
 Carlson, R., Anderson, M., Johnson, R., et al. 1999a, *Sci*, **283**, 2062
 Carlson, R., Calvin, W., Dalton, J., et al. 2009, in Europa, ed. R. T. Pappalardo, W. B. McKinnon, & K. K. Khurana (Tucson, AZ: Univ. Arizona Press), 283
 Carlson, R., Johnson, R., & Anderson, M. 1999b, *Sci*, **286**, 97
 Carlson, R. W. 1999, *Sci*, **283**, 820
 Cartwright, R. J., Nordheim, T. A., Cruikshank, D. P., et al. 2020, *ApJL*, **902**, L38
 Cassidy, T. A., Paranicas, C. P., Shirley, J. H., et al. 2013, *P&SS*, **77**, 64
 Chyba, C. F. 2000, *Natur*, **403**, 381
 Chyba, C. F., & Phillips, C. B. 2001, *PNAS*, **98**, 801
 Cooper, J. F., Johnson, R. E., Mauk, B. H., Garrett, H. B., & Gehrels, N. 2001, *Icar*, **149**, 133
 Dalton, J., Cassidy, T., Paranicas, C., et al. 2013, *P&SS*, **77**, 45
 Dalton, J., Prieto-Ballesteros, O., Kargel, J., et al. 2005, *Icar*, **177**, 472
 Danger, G., Ruf, A., Maillard, J., et al. 2020, *PSJ*, **1**, 55
 Dannenmann, M., Klenner, F., Böningk, J., et al. 2023, *AsBio*, **23**, 60
 Davis, M., Meier, R., Cooper, J., & Loeffler, M. 2021, *ApJL*, **908**, L53
 Ding, J., Boduch, P., Domaracka, A., et al. 2013, *Icar*, **226**, 860
 Filacchione, G., Adriani, A., Mura, A., et al. 2019, *Icar*, **328**, 1
 Freissinet, C., Millan, M., Glavin, D. P., et al. 2019, *P&SS*, **175**, 1
 Gerakines, P., Schutte, W., Greenberg, J., & van Dishoeck, E. F. 1994, *A&A*, **296**, 810
 Ghosh, J., Hariharan, A. K., Bhui, R. G., Methikkalam, R. R. J., & Pradeep, T. 2018, *PCCP*, **20**, 1838
 Gloer, A., Tóth, G., Ma, Y., et al. 2009, *JGRA*, **114**, A12203
 Goode, W., Kempf, S., & Schmidt, J. 2023, *P&SS*, **227**, 105633
 Grasset, O., Dougherty, M., Coustenis, A., et al. 2013, *P&SS*, **78**, 1
 Greenberg, R., Geissler, P., Hoppa, G., et al. 1998, *Icar*, **135**, 64
 Hand, K., & Carlson, R. 2012, *JGRE*, **117**, E03008
 Hand, K., & Carlson, R. 2015, *GeoRL*, **42**, 3174
 Hand, K. P., Carlson, R. W., & Chyba, C. F. 2007, *AsBio*, **7**, 1006
 Harris, C. D. K., Jia, X., Slavin, J. A., et al. 2021, *JGRA*, **126**, e28888
 Heymann, D. 2007, *IAsB*, **6**, 217
 Howell, S. M., & Pappalardo, R. T. 2020, *NatCo*, **11**, 1311
 Hsu, H.-W., Postberg, F., Sekine, Y., et al. 2015, *Natur*, **519**, 207
 Hudson, R. L., Gerakines, P. A., Yarnall, Y. Y., & Coones, R. T. 2021, *Icar*, **354**, 114033
 Jia, X., Kivelson, M. G., Khurana, K. K., & Kurth, W. S. 2018, *NatAs*, **2**, 459
 Jones, B. M., Kaiser, R. I., & Strazzulla, G. 2014, *ApJ*, **781**, 85
 Kammerer, P. A., Jr., & Lee, G. F. 1969, *EnST*, **3**, 276
 Khawaja, N., Postberg, F., Hillier, J., et al. 2019, *MNRAS*, **489**, 5231
 Khurana, K., Kivelson, M., Stevenson, D., et al. 1998, *Natur*, **395**, 777
 King, O., Fletcher, L. N., & Ligier, N. 2022, *PSJ*, **3**, 72
 Kivelson, M. G., Khurana, K. K., Russell, C. T., et al. 2000, *Sci*, **289**, 1340
 Klenner, F., Postberg, F., Hillier, J., et al. 2019, *RCMS*, **33**, 1751
 Klenner, F., Postberg, F., Hillier, J., et al. 2020a, *AsBio*, **20**, 179
 Klenner, F., Postberg, F., Hillier, J., et al. 2020b, *AsBio*, **20**, 1168
 Küppers, M., & Schneider, N. M. 2000, *GeoRL*, **27**, 513
 Li, J., Gudipati, M. S., Mishra, Y. N., Liang, M.-C., & Yung, Y. L. 2022, *Icar*, **373**, 114760
 Li, J., & Li, C. 2023, *Icar*, **394**, 115438
 Ligier, N., Poulet, F., Carter, J., Brunetto, R., & Gourgeot, F. 2016, *AJ*, **151**, 163
 Loeffler, M., Hudson, R., Moore, M., & Carlson, R. 2011, *Icar*, **215**, 370
 Loeffler, M., Raut, U., Vidal, R. A., Baragiola, R., & Carlson, R. 2006, *Icar*, **180**, 265
 Lv, X., Boduch, P., Ding, J., et al. 2014, *MNRAS*, **438**, 922
 Maillard, J., Carrasco, N., Schmitz-Afonso, I., Gautier, T., & Afonso, C. 2018, *E&PSL*, **495**, 185
 Mifsud, D. V., Kaňuchová, Z., Herczku, P., et al. 2021, *SSRv*, **217**, 14
 Mifsud, D. V., Kaňuchová, Z., Herczku, P., et al. 2022, *GeoRL*, **49**, e2022GL100698
 Mifsud, D. V., Kaňuchová, Z., Herczku, P., et al. 2023, *Icar*, **411**, 115926
 Miljković, K., Hillier, J., Mason, N., & Zarnecki, J. 2012, *P&SS*, **70**, 20
 Moore, M., & Hudson, R. 1998, *Icar*, **135**, 518
 Moore, M., & Hudson, R. 2000, *Icar*, **145**, 282
 Moore, M., & Khanna, R. 1991, *AcSpA*, **47**, 255
 Moore, M. H., Khanna, R., & Donn, B. 1991, *JGR*, **96**, 17541
 Napoleoni, M., Klenner, F., Hortal Sanchez, L., et al. 2023a, *ESC*, **7**, 1675
 Napoleoni, M., Klenner, F., Khawaja, N., Hillier, J. K., & Postberg, F. 2023b, *ESC*, **7**, 735
 Naseem, M., Neveu, M., Howell, S., et al. 2023, *PSJ*, **4**, 181
 Nordheim, T., Hand, K., & Paranicas, C. 2018, *NatAs*, **2**, 673
 Nordheim, T., Regoli, L., Harris, C., et al. 2022, *PSJ*, **3**, 5
 Oberg, K. I. 2016, *Chem. Rev.*, **116**, 9631
 O'Brien, D. P., Geissler, P., & Greenberg, R. 2002, *Icar*, **156**, 152
 Paranicas, C., Ratliff, J., Mauk, B., Cohen, C., & Johnson, R. 2002, *GeoRL*, **29**, 1074
 Petrik, N. G., Monckton, R. J., Koehler, S. P., & Kimmel, G. A. 2014, *J. Phys. Chem. C*, **118**, 27483
 Pilling, S., Duarte, E. S., Domaracka, A., et al. 2010, *A&A*, **523**, A77
 Pirronello, V., Brown, W., Lanzerotti, L., Marcantonio, K., & Simmons, E. 1982, *ApJ*, **262**, 636
 Postberg, F., Grün, E., Horanyi, M., et al. 2011a, *P&SS*, **59**, 1815
 Postberg, F., Kempf, S., Schmidt, J., et al. 2009, *Natur*, **459**, 1098
 Postberg, F., Khawaja, N., Abel, B., et al. 2018, *Natur*, **558**, 564
 Postberg, F., Schmidt, J., Hillier, J., Kempf, S., & Srama, R. 2011b, *Natur*, **474**, 620
 Poston, M. J., Carlson, R. W., & Hand, K. P. 2017, *JGRE*, **122**, 2644
 Roth, L., Saur, J., Retherford, K. D., et al. 2014, *Sci*, **343**, 171
 Rothard, H., Domaracka, A., Boduch, P., et al. 2017, *JPhB*, **50**, 062001
 Rubin, M., Jia, X., Altwegg, K., et al. 2015, *JGRA*, **120**, 3503
 Ruf, A., Bouquet, A., Boduch, P., et al. 2019, *ApJL*, **885**, L40
 Ruf, A., Bouquet, A., Schmitt-Kopplin, P., et al. 2021, *A&A*, **655**, A74
 Ruf, A., Kanawati, B., Hertkorn, N., et al. 2017, *PNAS*, **114**, 2819
 Schmitt-Kopplin, P., Gabelica, Z., Gougeon, R. D., et al. 2010, *PNAS*, **107**, 2763
 Souza-Corrêa, J., da Costa, C., & Da Silveira, E. 2019, *AsBio*, **19**, 1123
 Sparks, W., Hand, K., McGrath, M., et al. 2016, *ApJ*, **829**, 121
 Spencer, J. R., Tamppari, L. K., Martin, T. Z., & Travis, L. D. 1999, *Sci*, **284**, 1514
 Strazzulla, G., Baratta, G., Leto, G., & Gomis, O. 2007, *Icar*, **192**, 623
 Strazzulla, G., Garozzo, M., & Gomis, O. 2009, *AdSpR*, **43**, 1442
 Strazzulla, G., Palumbo, M., Boduch, P., & Rothard, H. 2023, *EM&P*, **127**, 2
 Tenelanda-Osorio, L. I., Bouquet, A., Javelle, T., et al. 2022, *MNRAS*, **515**, 5009
 Teolis, B., Plainaki, C., Cassidy, T., & Raut, U. 2017, *JGRE*, **122**, 1996

Thomas, E. C., Hodyss, R., Vu, T. H., Johnson, P. V., & Choukroun, M. 2017, [ESC](#), **1**, 14

Thomas, N., Bagenal, F., Hill, T. W., & Wilson, J. K. 2004, in *Jupiter. The Planet, Satellites and Magnetosphere*, ed. F. Bagenal, T. E. Dowling, & W. B. McKinnon (Cambridge Univ. Press) (Cambridge) 561

Trumbo, S. K., & Brown, M. E. 2023, [Sci](#), **381**, 1308

Trumbo, S. K., Brown, M. E., & Hand, K. P. 2019, [SciA](#), **5**, eaaw7123

Villanueva, G., Hammel, H., Milam, S., et al. 2023, [Sci](#), **381**, 1305

Waite, J. H., Glein, C. R., Perryman, R. S., et al. 2017, [Sci](#), **356**, 155

Ziegler, J. F., Ziegler, M. D., & Biersack, J. P. 2010, [NIMPB](#), **268**, 1818

Zolotov, M. Y., & Shock, E. L. 2004, [JGRE](#), **109**, E06003